JOINT EUROPEAN TORUS

JET–P(90)36

H. Weisen, D. Pasini, A. Weller , A.W. Edwards
and JET Team

Measurement of Light Impurity Densities and Z_{eff} in JET using X-ray Tomography

Measurement of Light Impurity Densities and Z_{eff} in JET using X-ray Tomography

H. Weisen[1], D. Pasini, A. Weller[2] , A.W. Edwards
and JET Team*

JET-Joint Undertaking, Culham Science Centre, OX14 3DB, Abingdon, UK

[1]CRPP, Association EURATOM-Confederation Suisse, Lausanne, Switzerland
[2]EURATOM-IPP Association, Garching, Germany
** See Appendix 1*

Preprint of Paper to be submitted for publication in
Nuclear Fusion

ABSTRACT.

In the vast majority of plasmas produced in the JET tokamak the X-ray emission at energies above about 1keV is dominated by Bremsstrahlung radiation from the background deuterium ions, and both Bremsstrahlung and recombination radiation from one or two light impurity species such as beryllium and carbon. Under these circumstances local values of impurity densities and concentrations, or alternatively of the effective charge Z_{eff} of the ion mixture, are derived from tomographic measurements of the local X-ray emissivity at energies above 1-3keV, in conjunction with measurements of electron density and temperature profiles. These calculations are performed using the intrinsic emissivities due to the impurity ions. The emissivities into the relevant energy bands, determined by the detector and filter characteristics, were calculated assuming coronal ionisation equilibrium, and tabulated as a function of electron temperature. This method offers a good spatial and temporal resolution, and is succesfully applied to most plasma conditions where the relative proportions of impurities are known. We also present a detailed sensitivity study to assess the effects of errors in the input data, and a comparison with established methods based on visible Bremsstrahlung measurements, and charge exchange spectroscopy.

Introduction

Plasma diagnostics based on broad-band emission of soft X-rays by the plasma are used on most fusion research devices, and applied to study magnetohydrodynamic phenomena, heat pulse propagation and impurity transport. Most devices are equipped with X-ray pinhole cameras having a fan of many viewing lines. The system on JET uses 38 viewing lines in a vertically oriented fan and 62 in a horizontal fan, providing a spatial resolution of about 7 cm[1] and a time resolution of 5 μs. The system is absolutely calibrated to within 1%, and allows tomographic reconstruction of X-ray emissivity profiles[2]. Many absorption filters are available to study the emission in different energy bands.

The X-ray emissivity from any ion species consists of Bremstrahlung, radiative recombination radiation and line radiation, and is proportional to the product of the ion and electron densities. At the electron temperatures of interest here ($T_e \geq 0.5$ keV) light impurities are highly ionised. Central electron temperatures obtained in JET are in the range 0.5-12 keV, depending on fuelling and heating conditions. Line radiation from light impurities emitted near the plasma edge is rejected by the beryllium absorption filters, which have cutoff energies in the range 1-4 keV, depending on their thickness. The resulting X-ray emission profiles are peaked, and allow for accurate determination of the local emissivity by tomographic inversion.

The dominant impurities are produced by sputtering at interface between the plasma and the material limiting surfaces. Until recently all limiting surfaces were made of graphite, resulting in carbon being the main contaminant, with oxygen second in importance. In 1989 beryllium was introduced, first only as thin (~0.1μm) coatings deposited by in-vessel evaporation, and later also in the form of solid limiters, X-point target plates and screens for the radio frequency heating antennae. Presently both beryllium and carbon surfaces are in the vacuum vessel, and the dominant impurity depends on which of those are in contact with the plasma. In some discharges both types are used, resulting in a mixture of beryllium and carbon impurities. In the near future all power handling surfaces in JET are expected to be beryllium components. Helium is sometimes used as a minority species for RF heating, or in ^{3}He-D fusion experiments, and needs to be considered for such discharges. Helium as a fusion product (ash) will also be present in D-T fusion experiments. Established quantitative diagnostics for light impurity and deuterium ions in JET include visible Bremsstrahlung measurements, active

charge exchange spectroscopy, and neutron measurements[3-5].

In addition to the light impurities, a small amount of heavier impurities like Ni and Cl can be present. These are measured using for example the X-ray pulse height analyser[6], VUV and X-ray crystal spectrometers[7]. In most circumstances radiation from these accounts only for a few percent of the total detected X-ray radiation.

I. Calculation of light impurity densities and effective charge

The X-ray camera system measures line integrated signals, which are tomographically inverted to give local emissivity profiles. The local emissivity E = E(r) is related to the local plasma parameters by

$$E = \sum_z n_e n_z \varepsilon_z(T_e), \qquad (1)$$

where $n_z(r)$ and $n_e(r)$ are the ion and electron densities, and $T_e(r)$ the electron temperature. $\varepsilon_z(T_e)$ is the energy integrated spectral emissivity, for a temperature T_e, normalised with respect to n_e and n_z, after transmission through the filter, taking into account the spectral sensitivity of the detector diodes. Fig. 1 shows the overall spectral sensitivity of the system for three common thicknesses of the beryllium absorption filters. The decrease at high energy is due to the silicon diode detectors, of 300 μm thickness, which become gradually more transparent at energies above about 10 keV. In fig.2 we show the function $\varepsilon_z(T_e)$ over the range of interest (0.5-20 keV) for two of the filters and the relevant ion species. For comparison emissivities are also shown for nickel and chlorine.

For practical impurity density calculations we have tabulated these normalised emissivities (ε_z) as a function of T_e for 0.5 keV $\leq T_e \leq$ 20 keV. The calculations are described in detail in ref.8, and include continuum and line radiation from all ionisation stages, and were done assuming coronal equilibrium. This assumption is of little consequence as shown by comparisons of ionisation equilibrium calculations with and without transport effects[8]. Only line radiation from light impurities near the edge is significantly affected by transport effects. Line radiation from light impurities does not contribute to the measured emissivities since it is cut off by the Be filters. Line radiation was calculated with excitation rate coefficients in the $\bar{g}$-approximation[9] and Gaunt factors according to Mewe[10]. Calculations of the

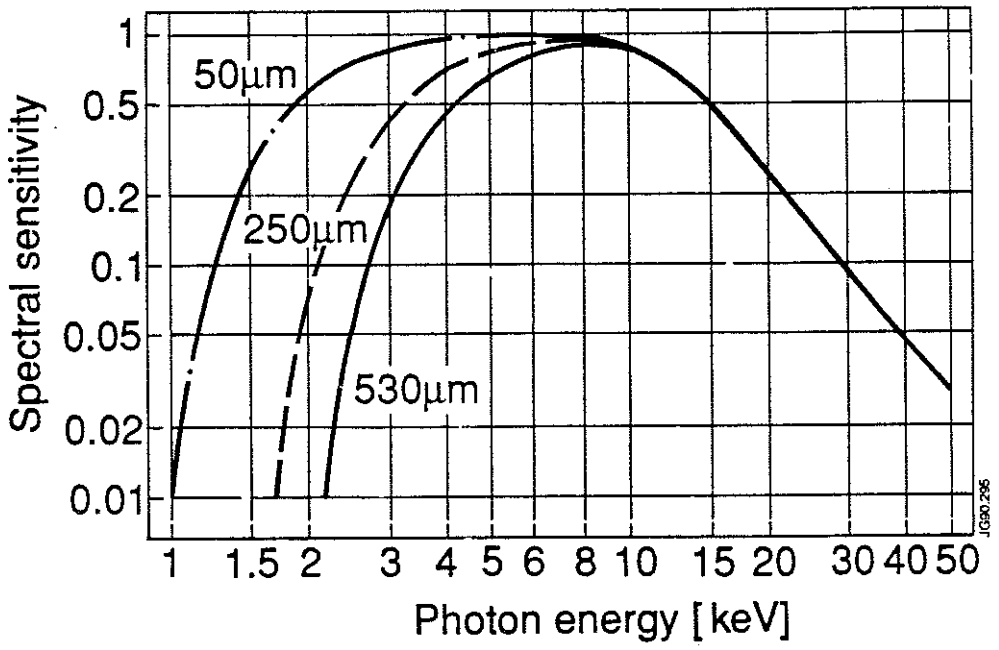

Fig. 1) Overall spectral sensitivity of JET soft X-ray cameras with three common thicknesses of the Be filters.

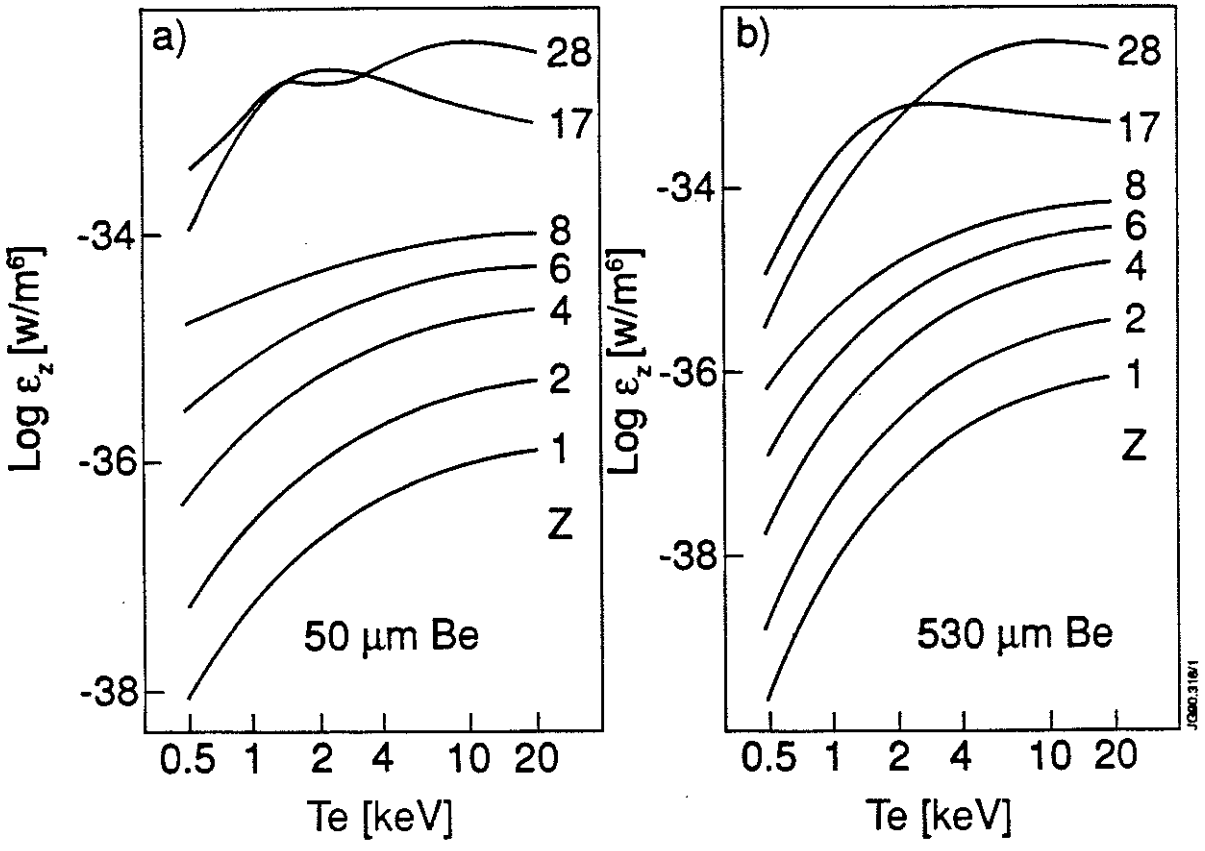

Fig. 2) X-ray emissivities for various ion species as function of electron temperature, integrated using the spectral sensitivity in fig.1 and normalised to n_e and n_z. Anotations refer to the nuclear charge. a) 50 μm Be filter. b) 530 μm Be filter.

continuum radiation were performed according to ref. 11. The spectral transmittance of the beryllium filters and silicon detector diodes was evaluated using the cross-sections tabulated in ref. 12.

In order to treat the case of more than one light impurity, it is convenient to define impurity proportions p_z by $n_z = p_z n_{imp}$, where $n_{imp} = \sum_{z \neq b} n_z$ is the overall density of impurity particles, excluding the background ion density n_b. Impurity proportions can be obtained from VUV spectroscopy and active charge exchange spectroscopy (CXS). From eq.(1), with the above definitions, the overall impurity concentration relative to the electrons, $c_{imp} = n_{imp}/n_e$, can be expressed as

$$c_{imp} = \frac{bE/n_e^2 - \varepsilon_b(T_e)}{\sum_z p_z [b\varepsilon_z(T_e) - z\varepsilon_b(T_e)]} . \qquad (2)$$

The effective ion charge (ion charge of a single ion species plasma with the same Bremsstrahlung emissivity) is obtained as

$$Z_{eff} = b + c_{imp} [\sum_{z \neq b} (z-b) z p_z] . \qquad (3)$$

II. Error propagation

Uncertainties arise from errors in the measured emissivity (E), electron densities and temperatures, and the measured or assumed impurity proportions. Because of the novelty of the approach described here, we present a detailed sensitivity study to errors in the input data. We find that both the sensitivities to errors in the electron temperature, and in the impurity proportions, are strongly dependent on the electron temperature. The large sensitivity at temperatures below about 1keV may make the method unsuitable for small devices. At electron temperatures of a few keV or more, which are obtained in the larger of the present devices, however, the relative sensitivities to errors in the electron temperature and impurity proportions are no larger than to those on the X-ray emissivity and the electron density.

Neglect of the contributions of high-Z species can be considered as resulting in an uncertainty on the measured emissivity if these are attributed to light impurities. When only one light ion species is to be considered, the linear error Δc_z on its concentration $c_z = n_z/n_e$ is obtained as

$$\Delta c_z = -[\gamma_b \varepsilon_b/(b\varepsilon_z - z\varepsilon_b) + c_z\gamma_z] \times \Delta T_e/T_e + [c_z + \varepsilon_b/(b\varepsilon_z - z\varepsilon_b)] \times [\Delta E/E - 2\Delta n_e/n_e] \quad (4)$$

where ΔT_e, Δn_e, and ΔE are the errors on T_e, n_e and E, and $\gamma_z(T_e) = d\ln\varepsilon_z/d\ln T_e$. γ_z plays the role of an exponent in a power law dependence and is strongly dependent on T_e (fig. 3). The high values of γ_z at low temperatures result from the high pass characteristics of the beryllium filters. A thicker filter has the advantage of rejecting more line radiation from medium and high-Z impurities. This advantage, however, comes at the price of a stronger dependence on T_e at low temperatures. This can be seen by comparing the filters with thickness of 50 and 530 μm in figures 2 and 3. As an increasing part of the continuous spectrum is transmitted at higher temperatures, γ_z is reduced. A limiting value for γ_z of 1/2 would be expected from the T_e dependence of the total Bremsstrahlung emission. In fact at high T_e, γ_z is reduced further due to the decrease of detector efficiency at photon energies above 10 keV (fig. 1).

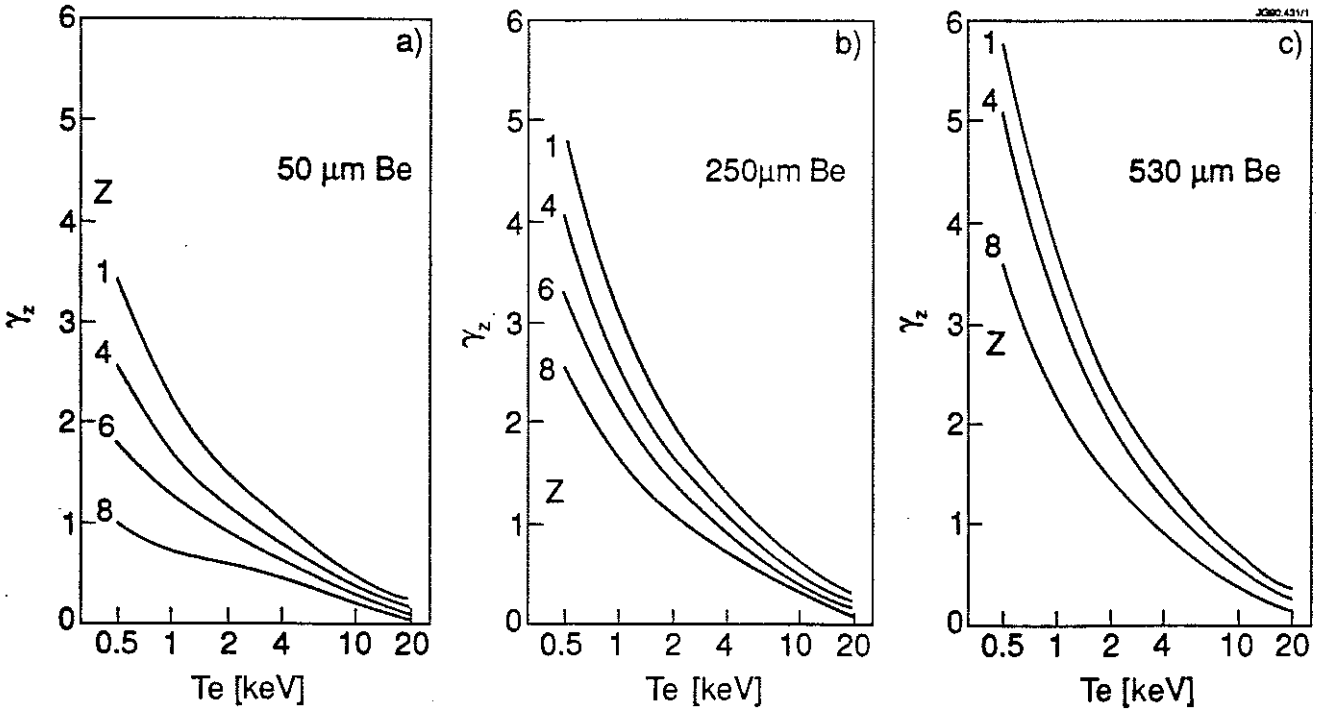

Fig. 3) Temperature sensitivity of emissivities expressed as $\gamma_z = d\ln\varepsilon_z/d\ln T_e$.
a) 50 µm Be filter, b) 250 µm Be filter, c) 530 µm Be filter.

Expression (4) contains terms that are independent of c_z and terms proportional to c_z. At low impurity concentrations ($c_z < \varepsilon_b/b\varepsilon_z$) the former effectively constitute a sensitivity limit given (with $b\varepsilon_z \gg z\varepsilon_b$ as is generally the case) by

$$|\Delta c_Z| \cong \varepsilon_b/(b\varepsilon_z) \times [\gamma_b |\Delta T_e/T_e| + 2|\Delta n_e/n_e| + |\Delta E/E|]. \quad (5)$$

At high impurity concentrations the relative uncertainty can be expressed as

$$|\Delta c_z/c_z| \cong \gamma_z |\Delta T_e/T_e| + 2|\Delta n_e/n_e| + |\Delta E/E|. \quad (6)$$

If, as a numerical example, obtained for a Be filter thickness of 250 μm, we assume a 10% uncertainty on T_e, and 5% on n_e and E, the sensitivity limit is 1.6×10^{-2} for beryllium and 5×10^{-3} for carbon at $T_e \cong 4$ keV. The relative error for large impurity concentrations is then about 25% and depends little on the species considered.

In the case when more than one impurity is present, significant errors on the deduced concentrations also result from errors or misestimates of their proportions. In the case of a mixture of two light impurities of charges z and w, the relative error on the concentration is given by $\Delta c_z/c_z = \Delta p_z/p_z + \Delta c_{imp}/c_{imp}$, where

$$\Delta c_{imp}/c_{imp} = \frac{-b\varepsilon_z + z\varepsilon_b + b\varepsilon_w - w\varepsilon_b}{p_z(b\varepsilon_z - z\varepsilon_b) + p_w(b\varepsilon_w - w\varepsilon_b)} \times \Delta p_z$$

$$= -\frac{1}{p_z + \rho_{zw}} \times \Delta p_z \sim \frac{1}{p_z + \varepsilon_w/\varepsilon_z} \times \Delta p_z \quad (7)$$

$$\text{with } \rho_{zw} = \frac{b\varepsilon_w - w\varepsilon_b}{b(\varepsilon_z - \varepsilon_w) + \varepsilon_b(w-z)}.$$

The auxiliary function $\rho_{zw}(T_e)$ is shown in fig.4 for three impurity pairs, carbon plus beryllium, beryllium plus helium, and oxygen plus carbon. Clearly errors on p_z can be enhanced by a factor of up to $\varepsilon_z/\varepsilon_w$.

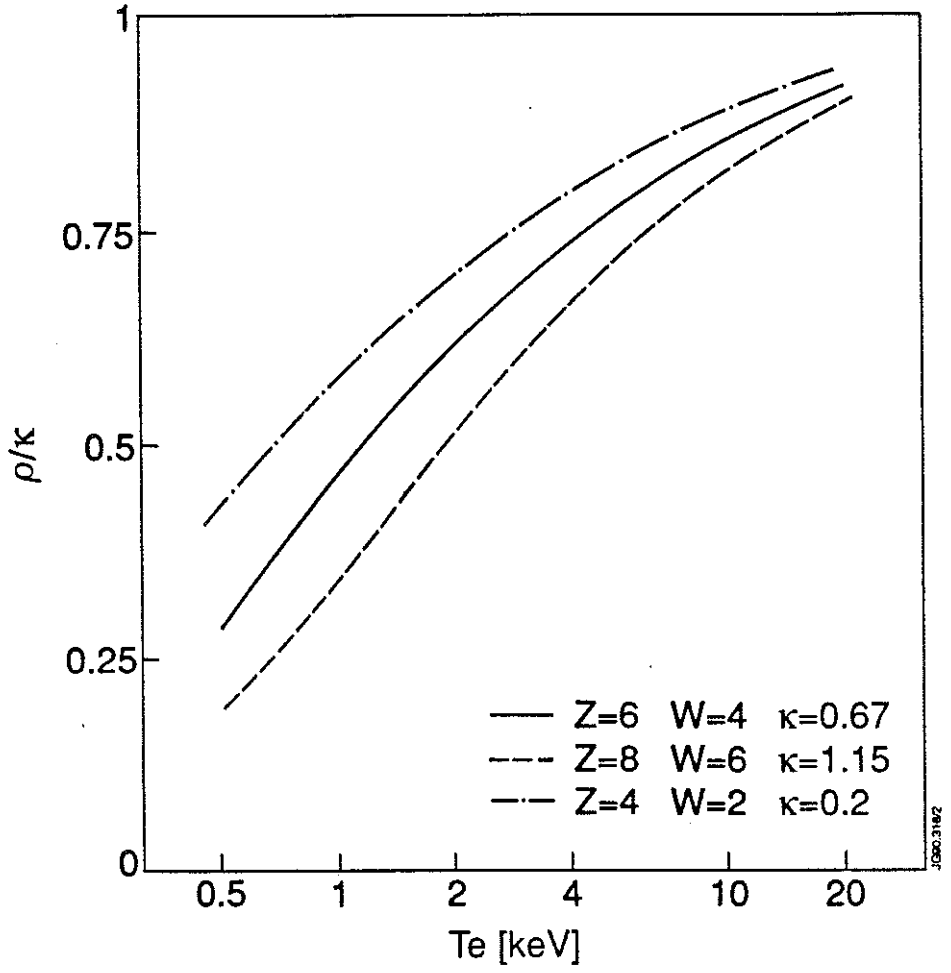

Fig. 4) Auxiliary function $\rho_{zw}(T_e)$ from eqs. (7) & (8), to evaluate effect of misestimate of impurity proportions on the measurement of c_{imp} and Z_{eff}. The curves shown are normalised to κ_{zw}, which are the values of ρ_{zw} for pure Bremsstrahlung. Note $\rho_{wz} = -\rho_{zw}-1$.

The expression of the impurity content in terms of the effective charge is less dependent, fortunately, on the impurity mixture. This is because at high temperatures the proportion of recombination radiation is reduced and the Z-dependence of the continuum radiation approaches that of ideal Bremsstrahlung. The largest departures occur at temperatures corresponding to energies near the 'recombination edge' of the light impurities. We may take

the quantity $\zeta = Z_{eff}$-b as a conventional measure of impurity concentration. An error Δp_z in the assumed proportions of the two impurities will then result in an error on ζ given by

$$\frac{\zeta + \Delta\zeta}{\zeta} = \frac{1 + \dfrac{\Delta p_z}{p_z + \kappa_{zw}}}{1 + \dfrac{\Delta p_z}{p_z + \rho_{zw}}} \quad . \tag{8}$$

where $\kappa_{zw} = \dfrac{(w\text{-}b)w}{(z\text{-}b)z - (w\text{-}b)w}$ is the equivalent of ρ_{zw} (eq. 7) for ideal Bremsstrahlung. Equation (8) holds for finite Δp_z. For small Δp_z equation (8) can be simplified to

$$\Delta\zeta/\zeta \cong \frac{\rho_{zw} - \kappa_{zw}}{(p_z+\rho_{zw})(p_z+\kappa_{zw})} \times \Delta p_z \quad . \tag{9}$$

As can be seen from equation (9) the resulting errors are dependent on the impurity proportions. Generally errors are smallest (largest) if the contribution of the lower charge impurity is misestimated in a plasma where the higher (lower) charge species dominates. This is also seen in fig. 5, showing $(\zeta+\Delta\zeta)/\zeta$ from equation (8) for different impurity pairs, for $|\Delta p_z|=0.2$ and in the case when the impurities are entirely mistaken for each other ($|\Delta p_z|=1$, fig.5a). At temperatures above 2 keV, in the worst case, a misestimate of $|\Delta p_z| = 0.2$ results in an error of 20% or less on ζ. At thermonuclear temperatures ($T_e \sim 10$ keV) this error is reduced to 10% or less, even if the two light impurities are entirely mistaken for each other.

III. Results

We have applied the method described to a large variety of discharge conditions. For the purpose of illustration we have selected two examples, representing extremes of electron temperature, electron density and plasma purity or contamination. The evolution of the tomographically inverted soft X-ray emissivity profile is shown in fig.6 for the first example. This reconstruction is based on Cormack's analytical solution[15] and includes the m=0 and m=1 poloidal harmonics, and the cos 2ϑ component of m=2 [2]. The

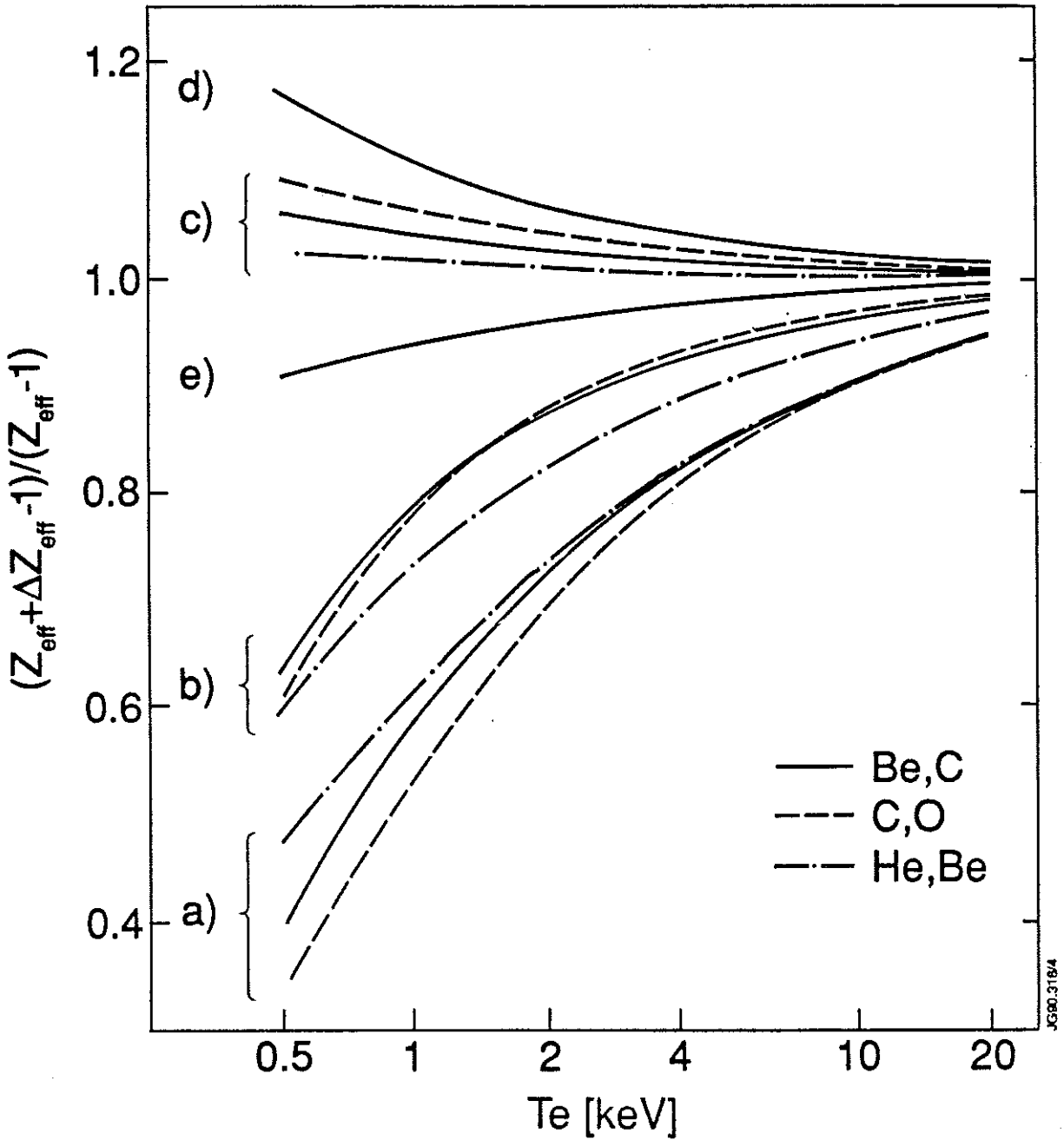

Fig. 5) Effect of misestimate of impurity proportions on $\zeta = Z_{eff}-1$ in a plasma with a mixture of two impurity species. The graph shows the ratio of measured to real values of ζ as a function of T_e. The different line types code for different impurity pairs (sodid: z=4, w=6, broken: z=6, w=8, broken-dotted: z=2, w=4).

a) $p_z = 0$, $p_w = 1$ *assumed in a plasma with* $p_z = 1$, $p_w = 0$, *with* $z < w$.

b) $\Delta p_z = -\Delta p_w = -0.2$ *assumed in a plasma with* $p_z = 1$, *for* $z < w$.

c) $\Delta p_z = -\Delta p_w = -0.2$ *assumed in a plasma with* $p_z = 1$, *for* $z > w$.

d) $p_z = 0.7$, *for z=6, assumed for a plasma with equal proportions of C and Be.*

e) $p_z = 0.3$, *for z=6, assumed for a plasma with equal proportions of C and Be.*

radial dependence is described using Zernike polynomials. In this discharge the application of 10 MW of radio frequency power led to a 3.5 s long sawtooth-free period ('Monster-sawtooth'), with central electron temperatures of up to 8 keV, as shown in fig 7. The figure also shows the central X-ray emissivities, and the derived values for Z_{eff} in the plasma center (R = 3.1 m), and at mid-radius (R = 3.6 m). This discharge was run on beryllium belt limiters, and beryllium was the dominant impurity. A beryllium to carbon density ratio of 5 to 1 was assumed in the calculation. Also shown is the line averaged value of Z_{eff} from visible Bremstrahlung (VB). The latter was obtained from the line integrated measurement of visible Bremstrahlung in a narrow wavelength band near 523 nm, using the measured electron density and temperature profiles, and assuming a constant Z_{eff} throughout the radius. (When the profile of Z_{eff} is not flat, a line average with a spatial weigthing proportional to $n_e^2 T_e^{-1/2}$ is obtained). Not surprisingly the agreement is best with the soft X-ray derived measurement when the profile of Z_{eff} is flat. In the early phase of the discharge when the Z_{eff} profile has a central peak, the line average value from VB is an underestimate of the central Z_{eff}.

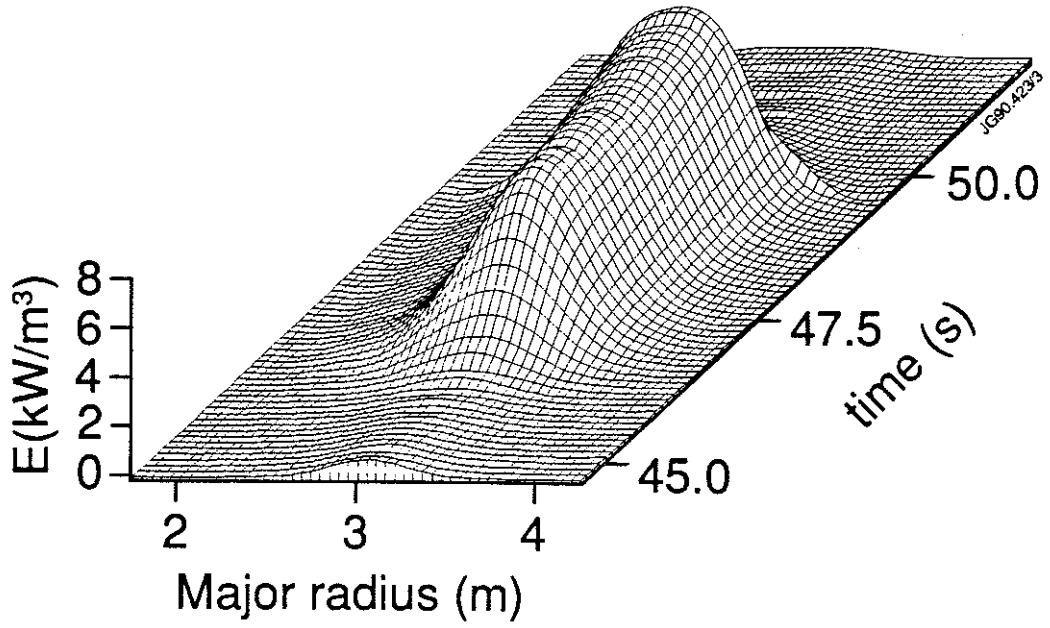

Fig. 6) Time evolution of emissivity profile.
250 μm Be filter, pulse no 20087

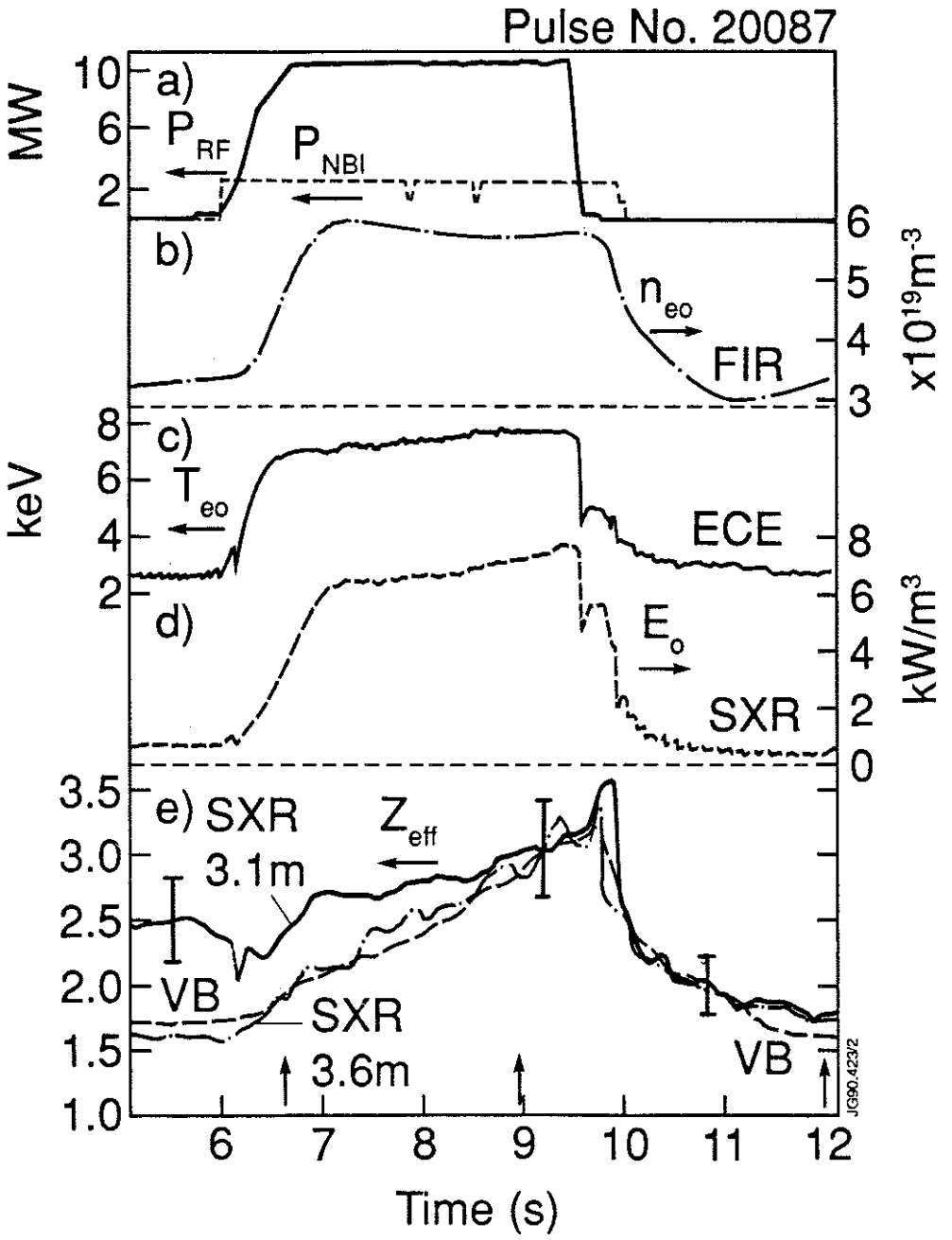

Fig. 7) Evolution of radio frequency heated discharge (pulse no 20087)

a) Radio frequency (P_{RF}) and neutral beam (P_{NBI}) power.

b) Central electron density from far infrared interferometry.

c) Central electron temperature from electron cyclotron emission (ECE).

d) Central X-ray emissivity, using a Be filter of 250 μm thickness.

e) Inferred values of Z_{eff} in the plasma centre (solid) and at mid-radius (broken-dotted). Broken line is line averaged Z_{eff} from visible Bremstrahlung.

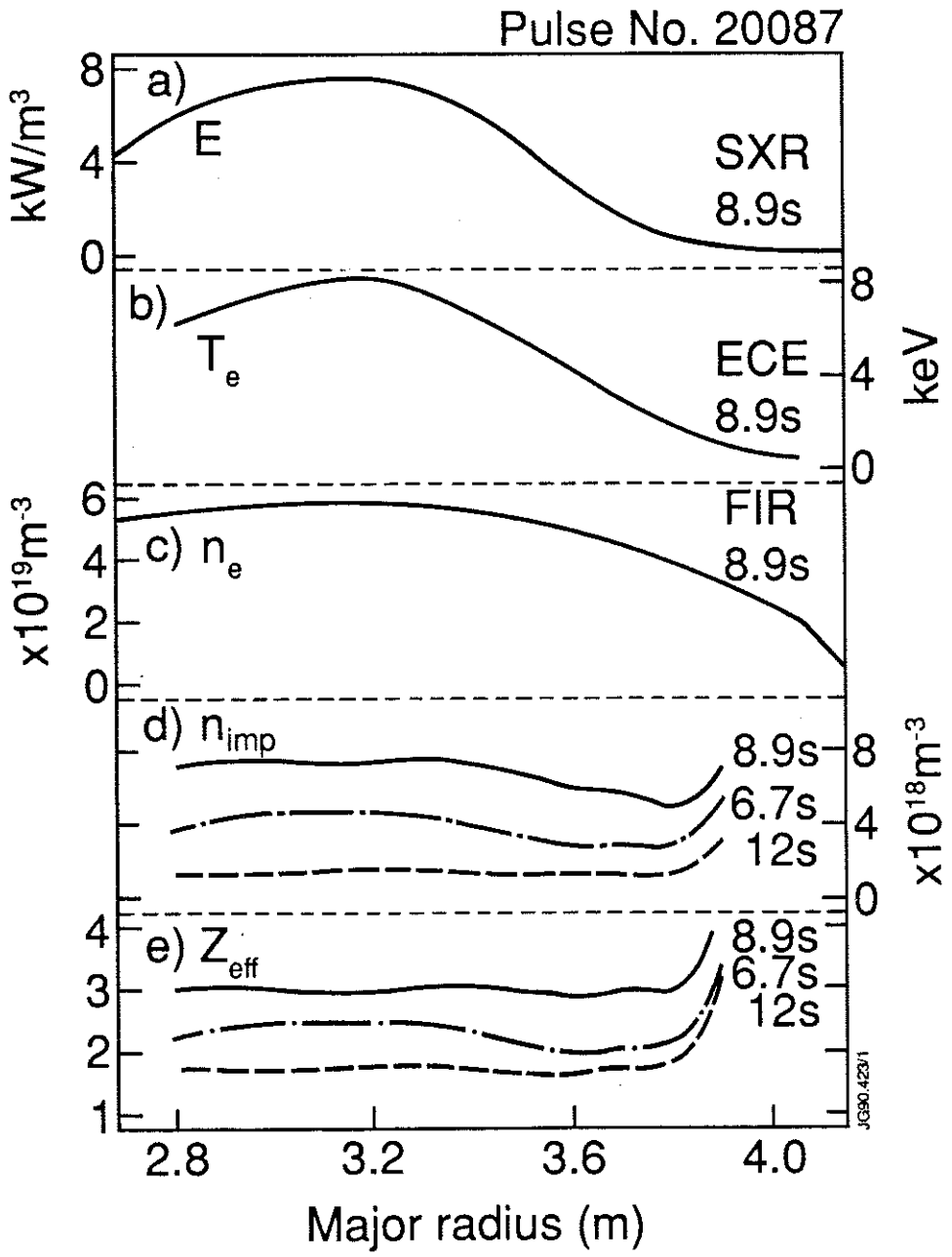

Fig. 8) Radial profiles (pulse no 20087)

a) Soft X-ray emissivity, b) Electron temperature from electron cyclotron emission, c) electron density from far infrared interferometry, d) corresponding impurity density profile (n_{imp} as defined in section I), e) corresponding profile of effective ion charge.

Fig.8 shows the radial profiles of emissivity, electron temperature and density near the end of the sawtooth-free phase, and the resulting ion density and Z_{eff} profiles. Also shown are profiles at the beginning of the sawtooth-free phase and during the ohmic phase after the heating pulse. Initially, during the current ramp (ending at 4 s), a peaked Z_{eff} profile was produced, which later relaxed to a remarkably flat profile. Such a relaxation, which may take several seconds, is also seen in purely ohmic discharges. The sharp increase of Z_{eff} and n_{imp} at 3.8 m is not real. This region is characterised by strong relative gradients of emissivity and temperature and even a small mismatch of the profiles can produce large errors. Also the emissivity at R=3.8 m is only a few percent of the central emissivity. At this level the tomographic inversion can be affected by aliasing from higher radial and poloidal harmonics, present in the real emissivity profile.

The second example, shown in figs.9 and 10, is that of an ohmic plasma into which a sequence of frozen deuterium pellets had been injected. As can be seen in fig.10a) the second pellet, which was injected at t = 5.5 s and penetrated to the plasma core, created a peaked electron density profile. The resulting emissivity profiles were extremely peaked, with a full width at half maximum of only 30 cm. The pellet brought the electron temperature well below 1 keV and flattened the impurity profiles at values of Z_{eff} barely above unity, as seen in fig.10b) and c). After the injection an impurity influx was seen (fig.9c and d), which lead to a profile of impurity density which was even more strongly peaked than the electron density profile (fig.10, t = 7.5 s). This central accumulation process is believed to be driven by the steep deuteron density gradients, as predicted by neoclassical theory. As the electron density relaxed back to a flat profile (t > 9 s), so did the profile of Z_{eff}. Electron temperature and density profiles from the JET Lidar Thomson scattering system[7] were used to calculate the profiles in fig.10. The apparent lobes at R=2.6 and 3.6m are artefacts of the reconstruction, as discussed above, and correspond to oscillations in the emissivity profiles of only 1% of the central emissivity. The impurity proportions (C:O:Cl:Ni ~ $0.75:0.25:10^{-3}:3\times10^{-3}$) used were obtained from VUV spectroscopy and from the pulse height analyser.

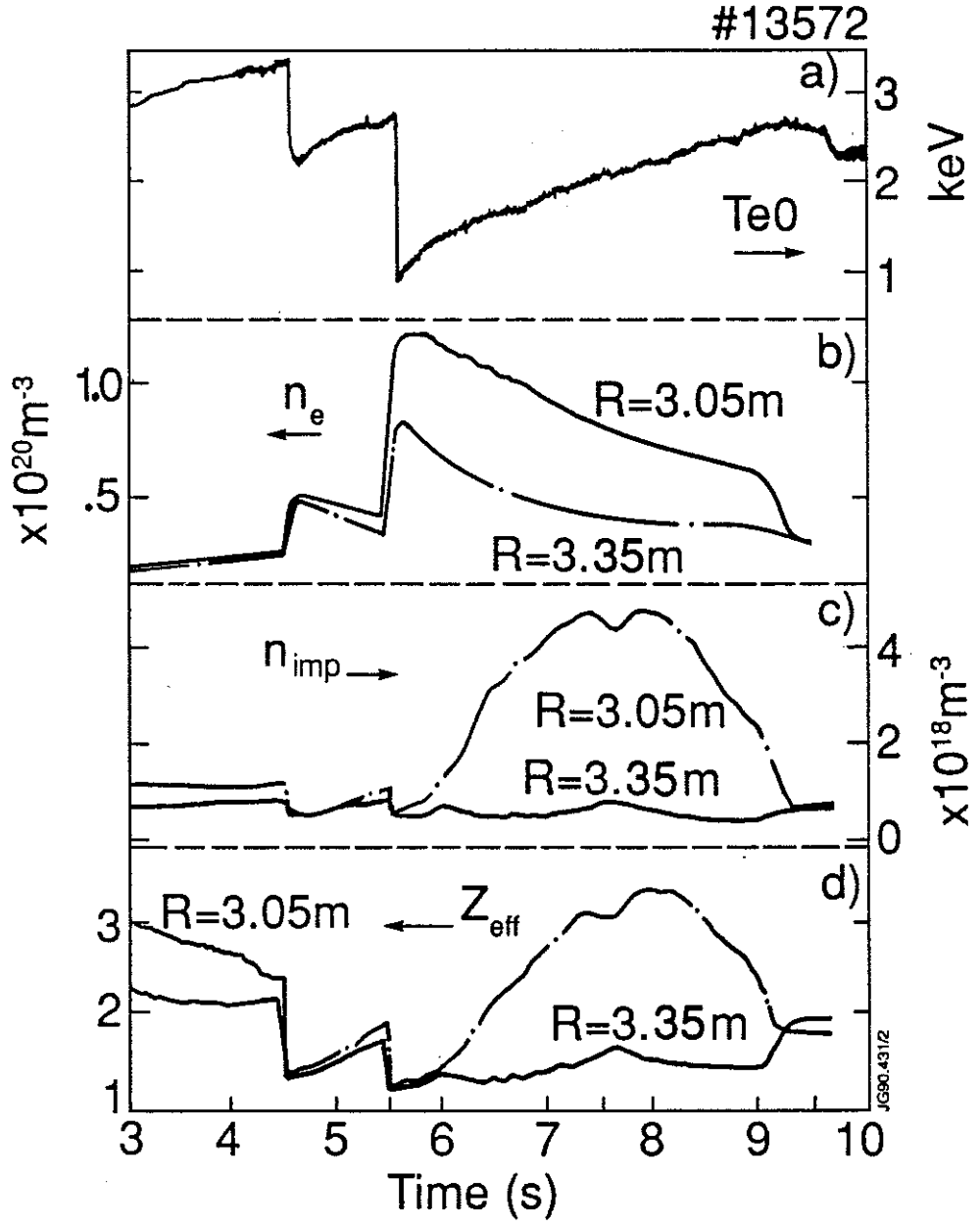

Fig. 9) Ohmic plasma with pellet injection (pulse no 13572).

a) Central electron temperature from ECE. b) Electron density from interferometry in the plasma centre and at 3.35 m. c) Impurity density, at R=3.05 and 3.35 m inferred from soft X-ray emissivity. d) Effective ion charge from soft X-ray emissivity. A Be filter thickness of 250 μm was used.

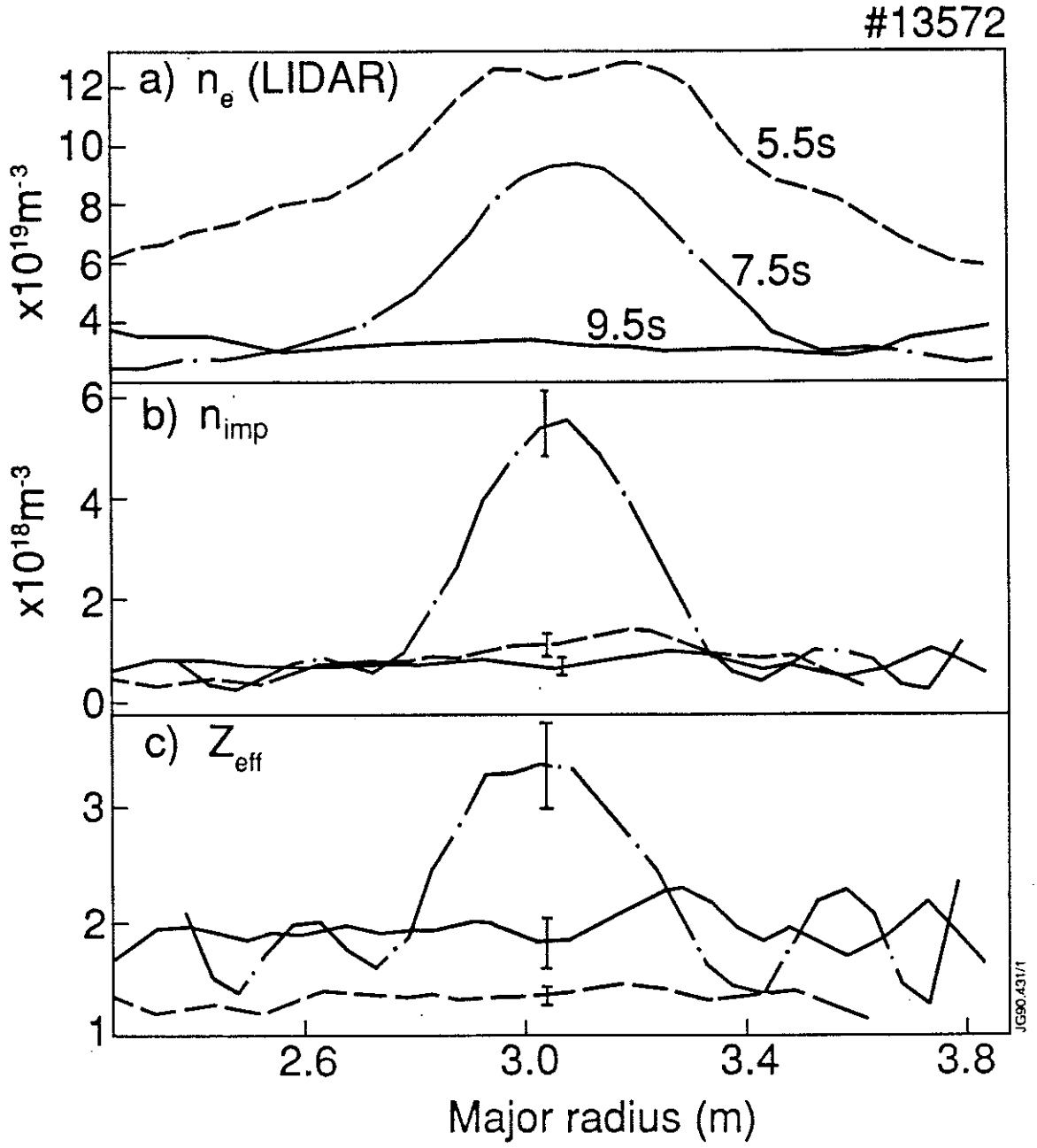

Fig. 10) Profiles in discharge with pellet injection (pulse no 13572).

a) Electron density from LIDAR Thomson scattering. b) Impurity density profile inferred from SXR and LIDAR. c) Profile of effective charge.

A general comparison of Z_{eff} measurements from X-rays with visible Bremsstrahlung (VB, fig.11) and with charge exchange spectroscopy (CXS, fig.12) shows good agreement between the three methods. The line average Z_{eff} from VB is representative of core conditions only in the case of flat Z_{eff} profiles. We therefore restricted the comparison shown in fig.11 to cases with Z_{eff} profiles (from SXR) which were flat to within 15% over the central half of the plasma. The different symbols refer to the two dominating impurities and correspond to different operational phases as explained in the introduction. The value of Z_{eff} from CXS (fig.12) was obtained by adding the contributions of the two dominating impurities according to eq.(3). In most of the data obtained after the introduction of Be into the JET vessel, both the carbon and beryllium concentrations were simultaneously measured in the plasma centre.

IV. Discussion

It is clear from the sensitivity study in section II that the accuracy of impurity densities and effective ion charges derived from soft X-ray emissivity measurements depends critically on the accuracy of electron temperature and density measurements. The obtainable accuracies (typically 25%) are however comparable to those of the other two main diagnostics for impurity densities used on JET, visible Bremsstrahlung (VB) and active charge exchange spectroscopy (CXS). Both of these depend on the accuracy of notably the electron density, and on the knowledge of the window transmission, which can become partially coated from exposure to the plasma during an operational period. Visible Bremsstrahlung measurements can occasionally be affected by spectral lines or by blackbody radiation from overheated limiting surfaces. A summary of the main advantages and disadvantages of the three methods is presented in table I.

The strong temperature dependence of X-ray emissivities at temperatures below 2 keV may explain why absolute measurements of impurity densities or Z_{eff} using this technique have not been reported from smaller devices with lower temperatures than JET. At low electron temperature, measurements based on Bremstrahlung emission in a narrow band in the visible or near infrared[13], with emissivities proportional to $T_e^{-1/2}$, may be preferable. In principle the temperature sensitivity of soft X-ray measurements could also be reduced by narrowing the bandwidth of the detected radiation, e.g. by using thinner

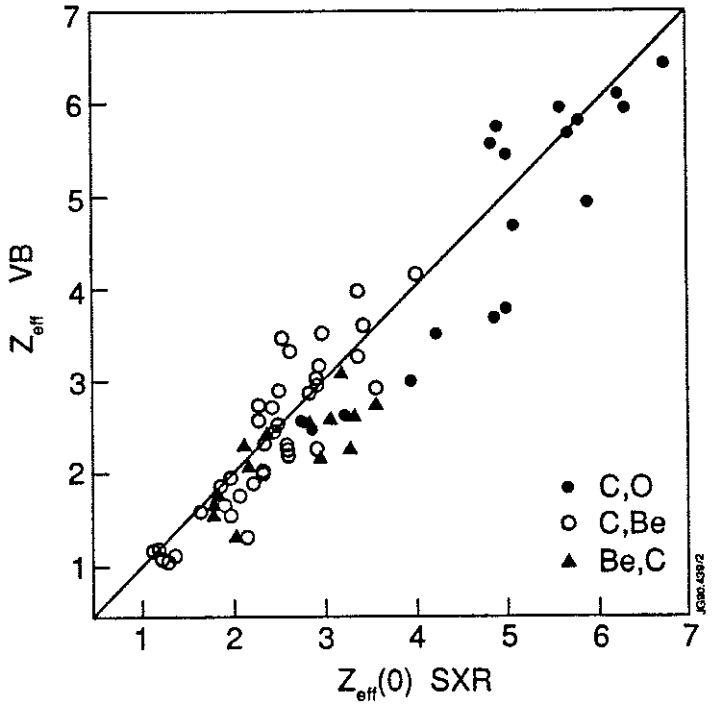

Fig. 11) Line average Z_{eff} from visible Bremsstrahlung versus central Z_{eff} from soft X-ray tomography. The comparison was restricted to cases with flat Z_{eff} profiles. Symbols indicate dominant impurities.

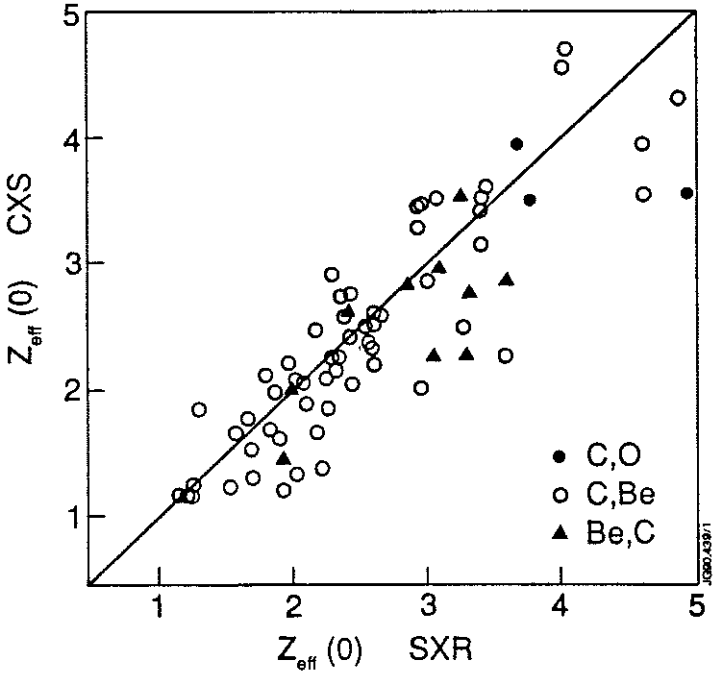

Fig. 12) Z_{eff} inferred from charge exchange spectroscopy of light impurities in the plasma centre versus central Z_{eff} from X-ray tomography. Symbols indicate dominant impurities.

detector diodes or low pass absorption filters to reject high energy photons in combination with Be high pass filters. Z_{eff} profile measurements from visible (or near infrared) Bremsstrahlung and soft X-rays have different characteristics. Narrow-band visible Bremstrahlung emissivity profiles are hollow in the case of flat or hollow density profiles, as frequently observed in H-mode plasmas, resulting in large uncertainties for the central values obtained from profile inversion procedures. The required inversions are also labour intensive, and normally only produced for discharges of particular interest. Only line averaged estimates for Z_{eff} from visible Bremsstrahlung are routinely available at JET. On the other hand X-ray emissivities for the Be filters used are peaked, allowing accurate central measurements. Uncertainties however increase towards the periphery as a result of the lower edge temperatures. Another drawback is that the low peripheral X-ray emissivities are susceptible to aliasing errors introduced by the tomographic reconstruction. These may result from higher poloidal harmonics not included in the inversion, due to plasma triangularity, or to higher radial harmonics when steep gradients are present. Steep gradients are observed in H-mode plasmas and with pellet - peaked profiles, and lead to small-scale oscillations on the reconstructed emissivity profiles. Such difficulties are however not intrisic to the method we describe and can be avoided by more suitable inversion techniques, some of which are presented in refs.[2] and [16].

Charge exchange measurements[4] of local impurity densities depend on calculations of the local neutral beam intensity. These require knowledge of the stopping cross sections for background and impurity ions, and the electron density profile. Large uncertainties can result at high densities, where the beams are strongly attenuated before they reach an observation volume in the plasma centre. In JET uncertainties on impurity densities resulting from beam attenuation can be estimated to exceed 30% in the plasma centre for line average electron densities above about $4\times10^{19}m^{-3}$. It should be noted however that a sensitivity limit in the sense of eq.(5) does not, in practice, exist for CXS measurements. Also, direct measurements of impurity concentrations can be expected when simultaneous CXS measurements of impurity and background ions will become available at JET. One particular problem, due to the weak CXS signals resulting from excessive beam attenuation at high density, is likely to subsist. In such conditions the observed signals can contain a significant contribution of radiation from 'plumes' of hydrogen-like ions produced by charge exchange reactions outside the observation volume which subsequently drift into the line of sight. Unless taken into account, the plume

contribution can lead to an overestimate of the impurity density. Another drawback of CXS is that the analysis of the spectra can be very labour intensive when the parameters of the charge exchange line have to be extracted from a complex spectrum of lines.

Given the difficulties associated with impurity measurements, the introduction of a new method based on soft X-ray emission is in itself valuable addition. Moreover, it presently the only method at JET that can provide measurements of impurity contamination of the core in virtually all plasma conditions. This method also has an intrinsically high time resolution, suitable for the study of transient events. (In the results presented in the previous section the time resolution was limited by the fairly poor time resolution of the electron density data.) With the planned introduction of real time tomography at JET[14], Z_{eff} profiles will be available to experimenters immediately after a discharge, or even in real time. Combinations with existing methods may also prove fruitful. Since CXS measurements of impurity proportions are independent of the density of injected neutrals, it can be combined with CXS to supply species-resolved impurity densities at electron densities beyond the reach of CXS alone. Where degradation of window transmittance is a concern, soft X-ray measurements can provide a cross check for absolute calibration, and even a recalibration.

The method also has potential for a device of the size of a fusion reactor if the sensitive detectors can be shielded against the high levels of gamma rays and neutrons. At thermonuclear temperatures this method has negligible sensitivity to uncertainties in the electron temperature and impurity mixture.

Conclusions

We have shown that the tomographically reconstructed X-ray emissivity can be used to provide impurity density or of the effective ion charge profiles. The method also requires accurate measurements of the electron density and temperature profiles, and a fair knowledge of the impurity mixture, all of which are available on the JET tokamak. It has a good intrinsic temporal and spatial resolution, and is applicable to virtually all plasma conditions with electron temperatures above a few hundred eV. The sensitivity of the inferred

Z_{eff} to errors in the electron temperature and the impurity proportions is largest at low temperatures, but decrease rapidly at high temperatures. We obtain good agreement with measurements of impurity contamination using visible Bremsstrahlung and charge exchange spectroscopy. Over visible Bremstrahlung based methods this approach has the advantage of peaked emissivity profiles, allowing for accurate measurements in the central region of the plasma. Over charge exchange spectroscopy it has the advantage of not depending on the presence of a neutral beam, and of being applicable to densities where the neutrals are excessively attenuated before they reach the plasma centre. The method is suitable for automated analysis, which makes it an attractive diagnostic for large scale fusion research devices.

Acknowledgements.

We gratefully acknowledge our many colleagues who made freely available the data on electron temperature and density used in the calculations of impurity densities, as well as measurements of impurity contamination by different methods. We would particularly like to thank Dr P.D. Morgan and Dr M. von Hellermann for stimulating discussions and valuable comments on this paper. This work was partly supported by the Swiss National Funds for Scientific Research.

Table I. Comparison of advantages (A) and disadvantages (D) of three different methods to measure the profile of Z_{eff} or impurity concentrations.

Soft X-ray tomography	**Visible Bremstrahlung**	**Charge exchange spectroscopy**
(A) Good central accuracy in most conditions due to peaked emission, even with hollow n_e profiles.	(D) Poor central accuracy with hollow profiles of VB emission.	(D) Density range for central measurements restricted by NBI attenuation (†). Dependent on availability of NBI.
(D) Unsuitable for measurements in plasma periphery.		(A) Good measurements in plasma periphery in most conditions.
(D) Requires knowledge of impurity mixture at low T_e.	(A) Does not require knowledge of impurity mixture.	(A) Does not require knowledge of impurity mixture.
(D) Unsuitable for plasmas with strong contamination by high-Z impurities.	(A) Insensitive to impurity charge.	(A) Measurement of low-Z impurities not affected by high-Z impurities.
(A) Independent of window transmission.	(D) Window transmission is major uncertainty on absolute calibration.	(D) Window transmission is major uncertainty on absolute calibration.
(D) Tedious calibration.	(A) Easy calibration.	(A) Easy calibration.
(A) Insensitive to radiation from hot material surfaces.	(D) Can be affected by blackbody radiation from hot surfaces.	(A) Insensitive to blackbody radiation.
(D) Strong sensitivity to errors on T_e at low T_e.	(A) Weak sensitivity to errors on T_e.	(A) Weak sensitivity to errors on T_e.
(A) Good time resolution (< 0.1 ms).	Moderate time resolution.	(D) Limited time resolution (≥ 10 ms).
(D) Sensitive to errors on n_e.	(D) Sensitive to errors on n_e.	(D) Sensitive to errors on n_e.
(D) Fairly expensive (multi-purpose diagnostic).	(A) Inexpensive.	(A) Fairly inexpensive if NBI available (multi-purpose diagnostic).

† May not apply to simultaneous CXS measurements of impurities and background ions.

References.

[1] Edwards A W, Fahrbach H U, Gill R D, Granetz R, Oord E, Schramm G, Tsuji S and Zasche D , Rev. Sci. Instrum. **57**, 2142 (1986).

[2] Granetz R S and Smeulders P, Nucl. Fusion **20**, 457 (1988).

[3] Morgan P D, 15th European Conference on Controlled Fusion and Plasma Heating, Europhysics Conference Abstracts, Vol 12B, Part 1, 139 (1988).

[4] Von Hellermann M G, Mandl W, Summers H P, Weisen H, Boileau A et al, Proceedings of the 8th Topical Conference on High Temperature Plasma Diagnostics, Cape Cod 6-10.5 1990, to be published in Rev. Sci. Instrum (1990), and references therein.

[5] Jarvis O N, Adams J M, Balet B, Conroy S, Cordey J G et al, Nucl. Fusion **30**, 307 (1990).

[6] Pasini D, Gill R D, Holm J, Van der Goot E, Rev.Sci.Instrum.**59**,693 (1988)

[7] Orlinskij D V, Magyar G, Nucl. Fusion **28**, 611 (1988) and references therein.

[8] Weller A, Pasini D, Edwards A W, Gill R D, Granetz R, JET report JET-IR(87)10, (1987).

[9] De Michelis C and Mattioli M, Nucl. Fusion **21**, 677 (1981).

[10] Mewe R, Astron. and Astrophys. **20**, 215 (1979).

[11] von Goeler S, Stodiek W, Eubank H, Fishman H, Grebenshchikov S, Hinnov E, Nucl. Fusion **15**, 301 (1975).

[12] Veigele W J, Atomic Data Tables **5**, 511 (1973).

[13] Röhr H, Steuer K H, and the ASDEX Team, Rev.Sci.Instrum. **59**, 1875 (1988).

[14] van der Goot E, Edwards A W, Holm J, Proceedings of the first International Conference on the Applications of Transputers, Liverpool University, August 1989, 306, IOS Press 1990, also JET report JET-P(89)45

[15] Cormack A M, J. Appl. Phys. **10**, 2908 (1963).

[16] Nagayama Y, Asakura N, Tsuji S, 14th European Conference on Controlled Fusion and Plasma Physics, Europhysics Conference Abstracts, Vol **11**, part III, 1306 (1987).

APPENDIX 1.

THE JET TEAM

JET Joint Undertaking, Abingdon, Oxon, OX14 3EA, U.K.

J.M.Adams[1], F.Alladio[4], H.Altmann, R.J.Anderson, G.Appruzzese, W.Bailey, B.Balet, D.V.Bartlett, L.R.Baylor[24], K.Behringer, A.C.Bell, P.Bertoldi, E.Bertolini, V.Bhatnagar, R.J.Bickerton, A.Boileau[3], T.Bonicelli, S.J.Booth, G.Bosia, M.Botman, D.Boyd[31], H.Brelen, H.Brinkschulte, M.Brusati, T.Budd, M.Bures, T.Businaro[4], H.Buttgereit, D.Cacaut, C.Caldwell-Nichols, D.J.Campbell, P.Card, J.Carwardine, G.Celentano, P.Chabert[27], C.D.Challis, A.Cheetham, J.Christiansen, C.Christodoulopoulos, P.Chuilon, R.Claesen, S.Clement[30], J.P.Coad, P.Colestock[6], S.Conroy[13], M.Cooke, S.Cooper, J.G.Cordey, W.Core, S.Corti, A.E.Costley, G.Cottrell, M.Cox[7], P.Cripwell[13], F.Crisanti[4], D.Cross, H.de Blank[16], J.de Haas[16], L.de Kock, E.Deksnis, G.B.Denne, G.Deschamps, G.Devillars, K.J.Dietz, J.Dobbing, S.E.Dorling, P.G.Doyle, D.F.Düchs, H.Duquenoy, A.Edwards, J.Ehrenberg[14], T.Elevant[12], W.Engelhardt, S.K.Erents[7], L.G.Eriksonn[5], M.Evrard[2], H.Falter, D.Flory, M.Forrest[7], C.Froger, K.Fullard, M.Gadeberg[11], A.Galetsas, R.Galvao[8], A.Gibson, R.D.Gill, A.Gondhalekar, C.Gordon, G.Gorini, C.Gormezano, N.A.Gottardi, C.Gowers, B.J.Green, F.S.Griph, M.Gryzinski[26], R.Haange, G.Hammett[6], W.Han[9], C.J.Hancock, P.J.Harbour, N.C.Hawkes[7], P.Haynes[7], T.Hellsten, J.L.Hemmerich, R.Hemsworth, R.F.Herzog, K.Hirsch[14], J.Hoekzema, W.A.Houlberg[24], J.How, M.Huart, A.Hubbard, T.P.Hughes[32], M.Hugon, M.Huguet, J.Jacquinot, O.N.Jarvis, T.C.Jernigan[24], E.Joffrin, E.M.Jones, L.P.D.F.Jones, T.T.C.Jones, J.Källne, A.Kaye, B.E.Keen, M.Keilhacker, G.J.Kelly, A.Khare[15], S.Knowlton, A.Konstantellos, M.Kovanen[21], P.Kupschus, P.Lallia, J.R.Last, L.Lauro-Taroni, M.Laux[33], K.Lawson[7], E.Lazzaro, M.Lennholm, X.Litaudon, P.Lomas, M.Lorentz-Gottardi[2], C.Lowry, G.Magyar, D.Maisonnier, M.Malacarne, V.Marchese, P.Massmann, L.McCarthy[28], G.McCracken[7], P.Mendonca, P.Meriguet, P.Micozzi[4], S.F.Mills, P.Millward, S.L.Milora[24], A.Moissonnier, P.L.Mondino, D.Moreau[17], P.Morgan, H.Morsi[14], G.Murphy, M.F.Nave, M.Newman, L.Nickesson, P.Nielsen, P.Noll, W.Obert, D.O'Brien, J.O'Rourke, M.G.Pacco-Düchs, M.Pain, S.Papastergiou, D.Pasini[20], M.Paume[27], N.Peacock[7], D.Pearson[13], F.Pegoraro, M.Pick, S.Pitcher[7], J.Plancoulaine, J-P.Poffé, F.Porcelli, R.Prentice, T.Raimondi, J.Ramette[17], J.M.Rax[27], C.Raymond, P-H.Rebut, J.Removille, F.Rimini, D.Robinson[7], A.Rolfe, R.T.Ross, L.Rossi, G.Rupprecht[14], R.Rushton, P.Rutter, H.C.Sack, G.Sadler, N.Salmon[13], H.Salzmann[14], A.Santagiustina, D.Schissel[25], P.H.Schild, M.Schmid, G.Schmidt[6], R.L.Shaw, A.Sibley, R.Simonini, J.Sips[16], P.Smeulders, J.Snipes, S.Sommers, L.Sonnerup, K.Sonnenberg, M.Stamp, P.Stangeby[19], D.Start, C.A.Steed, D.Stork, P.E.Stott, T.E.Stringer, D.Stubberfield, T.Sugie[18], D.Summers, H.Summers[20], J.Taboda-Duarte[22], J.Tagle[30], H.Tamnen, A.Tanga, A.Taroni, C.Tebaldi[23], A.Tesini, P.R.Thomas, E.Thompson, K.Thomsen[11], P.Trevalion, M.Tschudin, B.Tubbing, K.Uchino[29], E.Usselmann, H.van der Beken, M.von Hellermann, T.Wade, C.Walker, B.A.Wallander, M.Walravens, K.Walter, D.Ward, M.L.Watkins, J.Wesson, D.H.Wheeler, J.Wilks, U.Willen[12], D.Wilson, T.Winkel, C.Woodward, M.Wykes, I.D.Young, L.Zannelli, M.Zarnstorff[6], D.Zasche[14], J.W.Zwart.

PERMANENT ADDRESS

1. UKAEA, Harwell, Oxon. UK.
2. EUR-EB Association, LPP-ERM/KMS, B-1040 Brussels, Belgium.
3. Institute National des Récherches Scientifique, Quebec, Canada.
4. ENEA-CENTRO Di Frascati, I-00044 Frascati, Roma, Italy.
5. Chalmers University of Technology, Göteborg, Sweden.
6. Princeton Plasma Physics Laboratory, New Jersey, USA.
7. UKAEA Culham Laboratory, Abingdon, Oxon. UK.
8. Plasma Physics Laboratory, Space Research Institute, Sao José dos Campos, Brazil.
9. Institute of Mathematics, University of Oxford, UK.
10. CRPP/EPFL, 21 Avenue des Bains, CH-1007 Lausanne, Switzerland.
11. Risø National Laboratory, DK-4000 Roskilde, Denmark.
12. Swedish Energy Research Commission, S-10072 Stockholm, Sweden.
13. Imperial College of Science and Technology, University of London, UK.
14. Max Planck Institut für Plasmaphysik, D-8046 Garching bei München, FRG.
15. Institute for Plasma Research, Gandhinagar Bhat Gujat, India.
16. FOM Instituut voor Plasmafysica, 3430 Be Nieuwegein, The Netherlands.
17. Commissiariat à L'Energie Atomique, F-92260 Fontenay-aux-Roses, France.
18. JAERI, Tokai Research Establishment, Tokai-Mura, Naka-Gun, Japan.
19. Institute for Aerospace Studies, University of Toronto, Downsview, Ontario, Canada.
20. University of Strathclyde, Glasgow, G4 ONG, U.K.
21. Nuclear Engineering Laboratory, Lapeenranta University, Finland.
22. JNICT, Lisboa, Portugal.
23. Department of Mathematics, Univeristy of Bologna, Italy.
24. Oak Ridge National Laboratory, Oak Ridge, Tenn., USA.
25. G.A. Technologies, San Diego, California, USA.
26. Institute for Nuclear Studies, Swierk, Poland.
27. Commissiariat à l'Energie Atomique, Cadarache, France.
28. School of Physical Sciences, Flinders University of South Australia, South Australia SO42.
29. Kyushi University, Kasagu Fukuoka, Japan.
30. Centro de Investigaciones Energeticas Medioambientales y Techalogicas, Spain.
31. University of Maryland, College Park, Maryland, USA.
32. University of Essex, Colchester, UK.
33. Akademie de Wissenschaften, Berlin, DDR.

CR 88.49.1A